NanoImpact 3–4 (2016) 12–21

Contents lists available at ScienceDirect

NanoImpact

journal homepage: www.journals.elsevier.com/nanoimpact

# Relative quantitation of metal oxide nanoparticles in a cutaneous exposure model using enhanced darkfield microscopy and hyperspectral mapping

María del Pilar Sosa Idelchik, MD [a], Nicole M. Neu-Baker, MPH [a], Akshaya Chandrasekaran [a], Adam J. Friedman, MD [b], Mary D. Frame, PhD [c], Sara A. Brenner, MD, MPH [a,*]

[a] State University of New York (SUNY) Polytechnic Institute, College of Nanoscale Science, Nanobioscience Constellation, 257 Fuller Road, Albany, NY 12203, United States
[b] George Washington University School of Medicine and Health Sciences, Department of Dermatology, Ross Hall 2300 Eye Street NW, Washington, DC 20037, United States
[c] State University of New York (SUNY) Stony Brook, Department of Biomedical Engineering, Bioengineering Building, Stony Brook, New York 11794, United States

ARTICLE INFO

*Article history:*
Received 30 June 2016
Received in revised form 17 September 2016
Available online 23 September 2016

*Keywords:*
Histological samples
Nanomaterials
Imaging
Direct visualization

ABSTRACT

The biological effects associated with the unique properties of engineered nanoparticles (ENPs) remain largely unknown. Animal models of exposure are valuable for assessing potential toxicity and adverse health effects. This study presents a method to determine relative quantitation of nanoparticle (NP) abundance in histological samples in an ex vivo model of cutaneous exposure to metal oxide NPs using enhanced darkfield microscopy (EDFM) with hyperspectral imaging (HSI) and mapping. Porcine skin tissue was topically exposed to alumina, ceria, and silica NPs using a modified Franz diffusion chamber and histologically prepared for imaging. EDFM allowed for rapid direct visualization of NPs, while hyperspectral mapping confirmed the composition of NPs throughout the tissue, based on positive matching of pixels to reference spectral libraries (RSLs). Relative quantitation of NPs was achieved based on calculating the percentage of mapped pixels per field of view (FOV). The greatest abundance of mapped NPs was found in the ceria-exposed group regardless of tissue layer, relative to the other groups. Fewer NPs were found in the dermis compared to the *stratum corneum* in both the alumina- and ceria-exposed groups. This study demonstrated EDFM-HSI as a valuable method to determine relative quantitation of NPs in histological samples. The methods put forth in this study could be adapted for application to other NP types as well as other biological or environmental matrices.



## 1. Introduction

The rapid incorporation of engineered nanoparticles (ENPs) into consumer products and manufacturing processes necessitates investment in safe development, as the potential health effects associated with the unique properties of ENPs remain largely unknown (European Academies Science Advisory Council (EASAC), 2011; U.S. CDC-NIOSH, 2009; Oberdörster et al., 2005). In response, environmental and human health and safety research for nanotechnology is gaining momentum, investigating toxicity and biological effects that ENPs may have on living organisms and on ecosystems (Nel et al., 2015). It is imperative to proactively investigate the potential human health effects of occupational and/or consumer exposure to ENPs in order to guide their safe use, handling, and disposal (Contado, 2015; Shepard and Brenner, 2014a; Brenner and Neu-Baker, 2014; Singh and Nanda, 2014; Kessler, 2011).

Occupational settings present scenarios for potential worker exposure to nanoparticles (NPs) via inhalation and/or skin contact. The nanotechnology workforce is growing, with an estimated total of 2 million workers in the U.S. by 2020, with 6 million workers globally (Roco et al., 2010). Metal oxide and metal-based ENPs are increasingly used for industrial purposes and in consumer products: Research and Markets estimates over 1.6 million tons of metal oxide NPs will be incorporated into industries and technologies by 2020 (Global Industry Analysts, 2010). As such, developing direct visualization methods to assess NP location and abundance in skin tissue, as well as other biological and environmental models, is critical. Such methods development for nanoscale materials will aid in and facilitate related research efforts, including toxicology and exposures science.

Routes of potential human exposure to ENPs include inhalation, ingestion, injection, and cutaneous (skin) exposure (Oberdörster et al., 2005). Researchers are working to assess biological effects resulting from ENP exposure, and numerous studies utilizing different models for toxicological assessment of diverse NPs are underway (Krishnaraj

* Corresponding author at: State University of New York (SUNY) Polytechnic Institute, College of Nanoscale Science, Nanobioscience Constellation, 257 Fuller Road, Albany, NY 12203, United States.
*E-mail address:* sbrenner@sunypoly.edu (S.A. Brenner).

http://dx.doi.org/10.1016/j.impact.2016.09.006
2452-0748/

et al., 2016; Adamcakova-Dodd et al., 2014; da Silva et al., 2014; Fröhlich and Salar-Behzadi, 2014). Studies in the last decade have investigated the effects of cutaneous exposure to NPs (Schneider et al., 2009; Sykes et al., 2014; Baroli et al., 2007; Sonavane et al., 2008), primarily regarding exposure to zinc oxide (Zvyagin et al., 2008) and titanium dioxide (Adachi et al., 2013), which are commonly used in cosmetics and sunscreens. Other metal oxide NPs, such as aluminum oxide ($Al_2O_3$; alumina), cerium oxide ($CeO_2$; ceria), and silicon dioxide ($SiO_2$; silica), are commonly used by the semiconductor industry as abrasives during chemical mechanical planarization (CMP) polishing processes and may be accessible for worker inhalation or cutaneous exposure (Shepard and Brenner, 2014a, 2014b; Brenner and Neu-Baker, 2014; Brenner et al., 2016; Roth et al., 2015a).

In order to facilitate risk assessment for those who may be exposed to NPs, there is urgent need for faster, less expensive analytical methods that can identify, characterize, and quantify NPs in biological samples, while preserving the sample itself. ENPs in biological samples are commonly characterized and quantified through conventional methods, such as electron microscopy (EM) and spectrometry. These methods, while capable of providing valuable information in terms of identification, characterization, and quantitation, are typically costly, time-consuming, and destructive to the sample (Roth et al., 2015b; Vanhecke et al., 2014). The limitations of EM for analysis of NPs in biological samples, such as it being expensive and time consuming, have been discussed by Sosa Peña et al., (2016). While various spectrometry methods provide valuable quantitative information, other questions remain unanswered, such as the distribution of NPs within a specimen and the biological responses to NPs, which are more easily visually assessed in a histological sample. In contrast to spectrometry methods, enhanced darkfield microscopy with hyperspectral imaging (EDFM-HSI) can address these questions simultaneously, without requiring special markers or destruction of the sample.

EDFM with hyperspectral mapping has emerged as a method with high utility for rapidly identifying metal oxide and other NPs in complex matrices, including biological and environmental sample types (Sosa Peña et al., 2016; Roth et al., 2015c; Mortimer et al., 2014; Grabinski et al., 2013; England et al., 2015; Badireddy et al., 2012). While EDFM allows for simple and rapid direct visualization of high contrast structures in biological samples, the spectral angle mapper (SAM) feature of the HSI software (ENVI 4.8) offers automated spectral identification of the NPs of interest by mapping against a reference spectral library (RSL) created from a positive control sample. A spectral signature from the material of interest is created and used to identify the same material in other (experimental) samples. Once identification of the NPs is obtained through hyperspectral mapping, relative quantitative analysis is possible by calculating the pixels per area of interest or per field of view (FOV) that is occupied by the NPs of interest (Mortimer et al., 2014).

HSI has been widely utilized for clinical applications: for example, it has been used to discern between different types of carcinomas and other pathological conditions using histological samples obtained through biopsy (Darwiche et al., 2013). In these cases, the first step is to confirm the diagnosis through rigorous visual assessment by a pathologist in order to create an RSL to then map to other similar samples. The difference with NP-exposed tissues is that, up to now, there is no consensus on whether tissues present changes that are characteristic of a certain exposure; thus, the "pathologist-based diagnosis method" would not be a viable option. Moreover, and probably more importantly, when dealing with NPs, unless those NPs have a characteristic shape (e.g., multi-walled carbon nanotubes) or are an obvious addition to the sample (e.g., clear presence of NPs within the cell membrane limits and that are not present in an unexposed sample), their presence in a determined sample should be confirmed by an additional method in order to confidently create an RSL to further assess other samples (Sosa Peña et al., 2016). The case of metal oxide NP-exposed tissues is a particular one and its analysis challenges should be considered; for example, in histological samples, spherical metal oxide NPs have no uniform or distinctive shape (and may be present in aggregates/agglomerates, clusters, or dispersed as single NPs), and are often indistinguishable from common sample artifacts (Sosa Peña et al., 2016; Husain et al., 2015), thereby making the method based on a "visual determination" of NPs for the creation of RSLs an unsuitable one for this type of specimen. While the importance of utilizing a third method to confirm the presence of the material of interest for an accurate and reliable RSL for histological samples has been recently emphasized by Sosa Peña et al. (2016), this method is still rarely utilized by the HSI scientific community dealing with uncharacteristically shaped NPs in histological tissues.

Moreover, HSI has been utilized as both a semi-quantitative (Mortimer et al., 2014; Badireddy et al., 2012) and a quantitative tool (Klein et al., 2008; Aalderink et al., 2009) in both biological samples at a single cell level (e.g., protozoa) and in environmental samples (e.g., wastewater), as well as in non-biological samples (e.g., physical documents, such as 17th-century historical maps), respectively. While EDFM was utilized by Mercer et al., (2013) to quantify multi-walled carbon nanotubes (MWCNTs) in histological samples, their study neither utilized nor required HSI or mapping to achieve reliable results, since the characteristic shape of the MWCNTs permitted direct visualization and subsequent counting of structure; this, for instance, differs greatly from the uncharacteristic shape of metal oxide NPs that impedes the utilization of the same quantitation method based on visualization alone. Thus, when working with morphologically indistinct NPs, it is imperative to use both EDFM and hyperspectral mapping for identification and quantitation purposes. While "semi-quantitation" of spherical or morphologically indistinct NPs utilizing EDFM-HSI has been achieved at the cellular level as reported by Mortimer et al., (2014) where the NPs can be easily identified as dispersed high-contrast particles found enclosed within the cellular membrane, a similar quantitation of NP abundance in histological samples has not yet been achieved, as challenges arise when the NPs are found either in clusters or dispersed form, and when they do not respect cellular limits. Similarly, the methods used for complex waters (Badireddy et al., 2012), where the dispersed nature of the NPs makes it easier to identify their size and number, fail to be useful for histological samples for the reasons mentioned above. In contrast, the term "relative quantitation" is used to describe the methods presented in this study, as we compare higher or lower abundance between different groups.

For the analysis of histological samples exposed to metal oxide NPs with EDFM-HSI, we propose a method for HSI visualization, mapping, and relative quantitation of NPs that combines several approaches in an effort to strive for consistency and accuracy in sample analysis that could potentially become a much-needed standard for NP-containing histological tissue analysis. The combined approaches and techniques: 1) are similar to the traditional methods used in pathology for histological sample assessment, where the load of particles in multiple frames within a sample is averaged; 2) utilize the known methods for visual NP identification with EDFM where the properties of metal oxide NPs provide high contrast allowing for easier identification, without the need for markers or tissue destruction; 3) include confirmation of EDFM findings by assessing the presence of the NPs of interest by a third method (in this study, Raman spectroscopy and energy-dispersive X-ray spectroscopy) to create an accurate RSL (a step typically absent in other studies); 4) combine HSI and mapping of multiple samples based on an accurate and confirmed RSL; and 5) establish a method for relative quantitation of NPs in tissue samples based on mapped pixels per FOV.

While EDFM-HSI may not be in a position at present to usurp EM in terms of resolution, or spectrometry in terms of quantitation, it is capable – as a single tool – of providing a wealth of information from an intact biological sample, which could then be used for additional investigation by other methods. Additionally, it allows for faster image

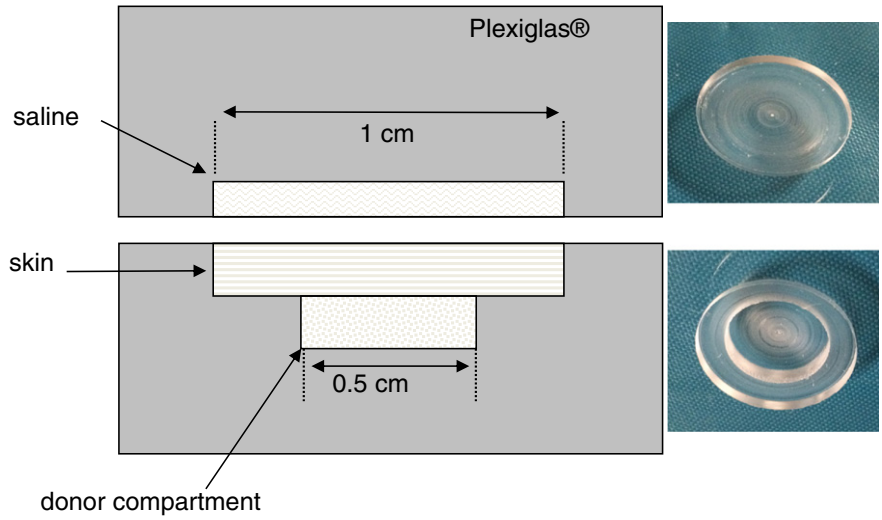


**Fig. 1.** Modified Franz diffusion chamber for ex vivo porcine skin exposures. Schematic of one modified Franz diffusion chamber. The inset photographs (taken at an angle to show depth) show the actual lower and upper chambers. Concentric holes provided the deeper donor compartment and shallower skin compartment in the lower Plexiglas® plate. A matching shallow compartment in the upper plate provided space for saline plus the remainder of the subcutaneous portion of the skin. On a single plate, 20 chambers were spaced 5 cm (rim to rim) apart. This spacing eliminated cross-contamination. By retaining the donor compartment below the skin, any diffusion occurring into the skin was not seepage, and against gravity. By using only the central part of the skin exposed to the donor compartment, and trimming away all skin not exposed, wicking of fluids around the skin to artificially place NP, was reduced.

acquisition, preservation of tissue integrity, reduced costs, and non-destructive sample preparation compared to conventional methods (Sosa Peña et al., 2016; Roth et al., 2015c; Mortimer et al., 2014).

The goal of this study is to present a non-destructive method for relative quantitative analysis of NPs in biological samples by combining EDFM and hyperspectral mapping, while also assessing biodistribution of metal oxide NPs within histological samples. This study also demonstrates the ease of visualizing NPs in histological samples using EDFM compared to conventional brightfield (BF) microscopy.

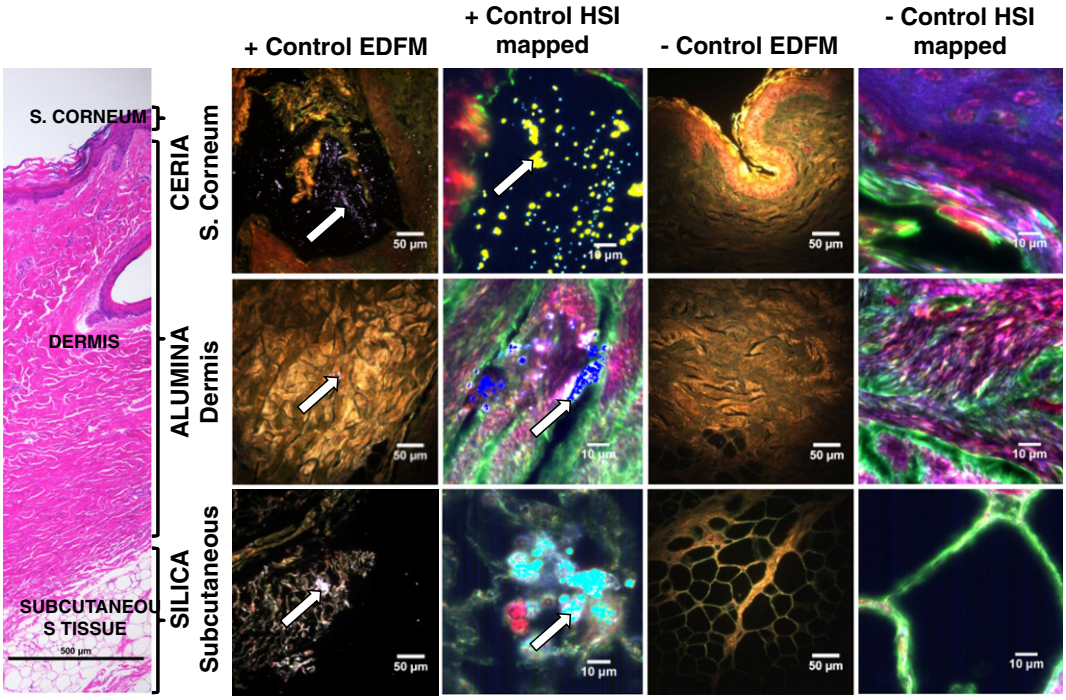


**Fig. 2.** Positive and negative controls mapped against RSLs. Rows correspond to the positive and negative controls of H&E stained skin samples mapped against the RSL created from ceria, alumina, and silica NPs in positive control tissues. A diagram of the skin layers is provided to the far left on an H&E stained sample, where brackets indicate each layer. The first two columns correspond to positive control samples imaged with EDFM (40× magnification) and HSI mapping (100× magnification), respectively. From top to bottom, *s. corneum* of a ceria-exposed sample (HSI positive mapping shown in yellow), dermis of an alumina-exposed sample (HSI positive mapping shown in blue) and subcutaneous tissue of a silica-exposed sample (HSI positive mapping shown in aqua). The third and fourth columns correspond to negative control samples images with EDFM (40× magnification) and HSI mapping (100× magnification), respectively. They correspond to the *s. corneum*, dermis, and subcutaneous tissue of a sample exposed to a solution with no NPs. No positive mapping is shown in the negative control samples. (Ceria images reprinted with permission (Sosa Peña et al., 2016, Wiley.)

## 2. Materials and methods

### 2.1. Metal oxide nanoparticles

Industrial metal oxide NP suspensions used for semiconductor wafer polishing were utilized in this study. These suspensions were comprised of alumina, ceria, or silica NPs, with dispersants, surfactants, and acids or bases in deionized water. Based on scanning electron microscopy analysis, the alumina NPs were approximately 71.5 nm in diameter; the ceria NPs were approximately 35 nm in diameter; and the silica NPs were approximately 49.5 nm in diameter (Badireddy et al., 2012). The NPs used in this study were further characterized, as previously reported, by scanning electron microscopy with energy-dispersive X-ray spectroscopy (EDX), dynamic light scattering (DLS), scanning mobility particle sizing (SMPS), inductively coupled plasma-optical emission spectrometry (ICP-OES), and single-particle inductively coupled plasma-mass spectrometry (SP-ICP-MS) (Roth et al., 2015d) (see Supplementary material Table S1).

### 2.2. Porcine skin exposure model

Porcine skin samples were topically exposed to industrial metal oxide NPs suspended in an aqueous solution in doses that are relevant to potential cutaneous occupational exposures in the semiconductor industry. Ex vivo skin samples were obtained from the dorsolateral region of 20 adult pigs, obtained through a tissue-sharing program at Stony Brook University (Stony Brook, NY) and approved by the Institutional Animal Care and Use Committee (IACUC) at Stony Brook University. Samples were cut into 1.5 cm long × 1.5 cm wide × 0.5 cm thick pieces to ensure visualization from the *stratum corneum* to the subcutaneous tissue. The samples were deposited within a modified Franz diffusion chamber (Fig. 1) designed by the Frame Lab specifically for these small volume exposures with a diffusional area of 0.785cm$^2$ where the epidermis, facing the donor compartment, was exposed to 75 μL of NP-containing solution for 24 h. The system was constructed of thick Plexiglas® plates with recessed donor and skin compartments. After filling the donor compartment with NP-containing solution, the skin was placed epidermis side down, and saline was dripped onto the subcutaneous surface. The matching compartment was laid over the skin and the two plates locked in place, with the donor compartment remaining below. The subcutaneous tissue faced a receptor compartment containing phosphate buffered saline (PBS) solution. The skin itself provided an adequate "gasket" to prevent drying out; only the central region of the skin exposed to the donor compartment was used for histology and imaging. The total exposure was 0.758 μg for alumina, 0.623 μg for ceria, and 8.858 μg for silica. The NP solutions used in this study were at the same concentration and the same composition as the commercial products used in the industry. A chemical fume hood was used for the exposures and room conditions were maintained at 23–25 °C and 50–60% humidity. From the 20 porcine models, multiple tissue samples were tested per pig. Experimental samples for topical exposure to NPs using the modified Franz chamber were collected from 15 pigs (5 alumina, 5 ceria, and 5 silica); 2 pigs were used as negative controls and were exposed to an aqueous solution without NPs in the donor compartment and PBS in the receptor compartment of the modified Franz chamber; the remaining 3 pigs were used as positive controls, each injected with the NP-containing solution (1 alumina, 1 ceria, and 1 silica). Injection of 10 μL volume at the same concentrations as exposed samples was via a tuberculin syringe placed 100 μm subcutaneous; these positive controls were used to create RSLs for hyperspectral mapping.

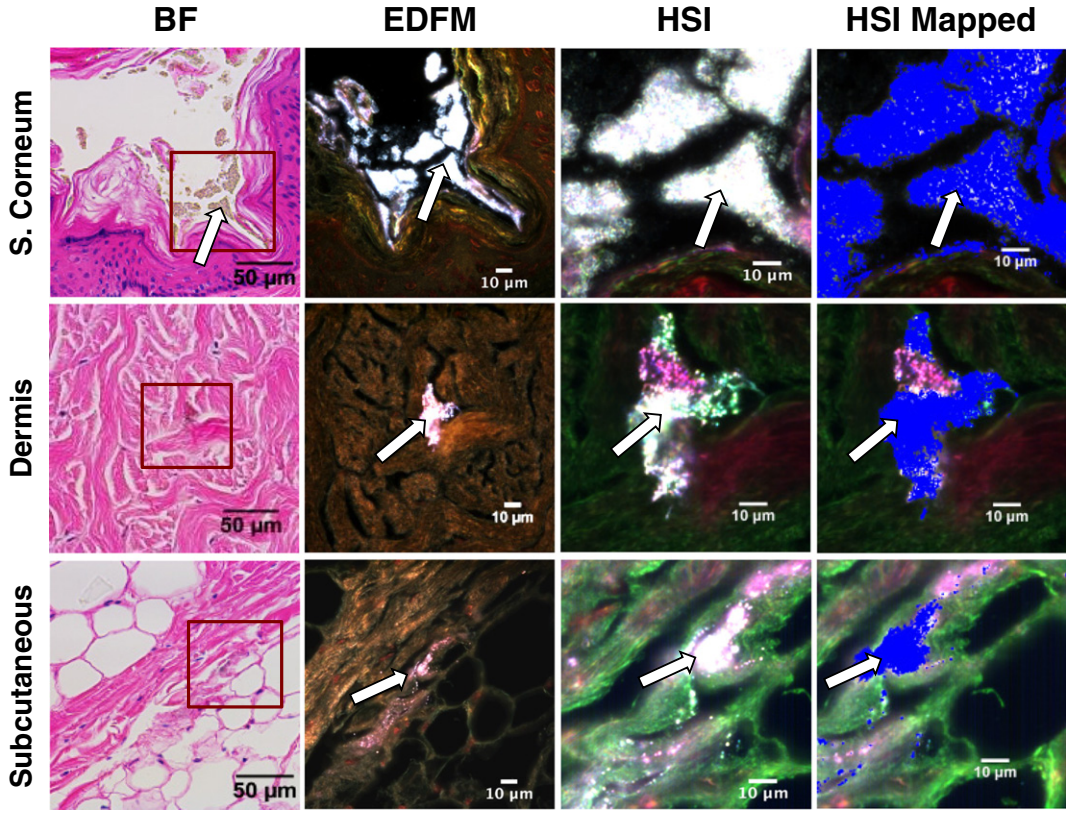


**Fig. 3.** Alumina nanoparticles in porcine skin. Alumina NPs are found in H&E stained skin samples and imaged with different modalities (from left to right: BF, EDFM, HSI, and HSI mapped overlay). From top to bottom, images correspond to *s. corneum*, dermis, and subcutaneous tissue of different samples in the alumina exposure group, respectively. In the brightfield (BF) column (40× magnification), while NPs are evident in the *s. corneum* they are not in the dermis and subcutaneous tissue. The areas enclosed in a red square were imaged with EDFM and HSI (100× magnification). White/pink high contrast areas (arrows) corresponding to the NPs are shown in EDFM and HSI, while positive mapping is represented by the blue overlay on the HSI mapped images.

### 2.3. Histological preparation

After exposure, the skin tissues were fixed by formalin immersion and histologically prepared by the Albert Einstein College of Medicine Histology and Comparative Pathology Facility (Bronx, NY) following commonly used methods (Roth et al., 2015b; Kumar & Kiernan, 2010; Titford, 2009). In short, formalin fixed tissues were processed to paraffin as described previously (Roth et al., 2015b) and were sectioned to a 6 μm thickness and directionally from subcutaneous to epidermal layer, using a clean blade for each cut, to minimize risk of artificially trafficking NPs in the direction of potential penetration. Samples were mounted onto glass microscopy slides, deparaffinized, rehydrated, and stained with hematoxylin and eosin (H&E) for visualization via BF microscopy for comparison to EDFM (Roth et al., 2015b; Kumar & Kiernan, 2010; Titford, 2009). While the histological H&E stain may have an effect on the spectral profile when compared to unstained samples when analyzed with EDFM-HSI, as long as the RSL is created from a positive control under the same preparation and staining conditions (as is the case in this study), it should not compromise the mapping results, while allowing for easier identification of structures with all the imaging modalities we utilized.

### 2.4. Enhanced darkfield microscopy (EDFM) and hyperspectral imaging (HSI)

A hyperspectral imaging system (CytoViva, Auburn, AL) mounted on an Olympus BX-43 microscope with an enhanced darkfield condenser was used for NP visualization in the skin samples. A DAGE optical camera and Exponent7 software were used for EDFM and a Pixelfly camera system and ENVI 4.8 software were used for HSI. Exposure settings were evaluated to determine which settings would provide with the best high contrast images under EDFM; a gain of 3.0 dB, shutter of 35 ms, and light source brightness of 75% were consistently used to examine the samples. After scanning the entirety of each sample, images of the highest NP-loaded areas were captured with EDFM and HSI in each cutaneous layer and in the subcutaneous tissue. Under EDFM, suspected NPs of interest were detected as high contrast areas within the tissue. In each cutaneous layer and subcutaneous tissue, 4 different areas with the highest load of suspected NPs were captured with EDFM and hyperspectral datacubes (hyperspectral images that can be analyzed with SAM) were captured of the same areas for mapping purposes. A total of 20 datacubes were obtained per tissue layer per exposure group. Positive and negative control samples were imaged following the same steps. EDFM images were taken at 10× (air), 40× (air) and 100× (oil immersion) magnification, while hyperspectral datacubes were captured at 100× (oil immersion), using 0.25 s exposure time, 720 lines, and high spatial resolution to create datacubes with a total of 1,000,848 pixels (64 $nm^2$ each) for a total FOV area of 0.004 $mm^2$.

### 2.5. Hyperspectral mapping

For spectral mapping analysis, spectral libraries (SLs) containing spectra for NPs were obtained from the positive control datacubes and then filtered against negative control datacubes to remove duplicative spectra, creating a RSL for each type of NP (alumina, ceria, and silica). The RSL for each NP was used to map the positive and negative control samples to verify either presence or absence of the NPs of interest, and subsequently, all the experimental samples. Three datacubes were obtained for each of the positive control samples. From these datacubes, three SLs were produced for each type of NP. The three SLs for a specific

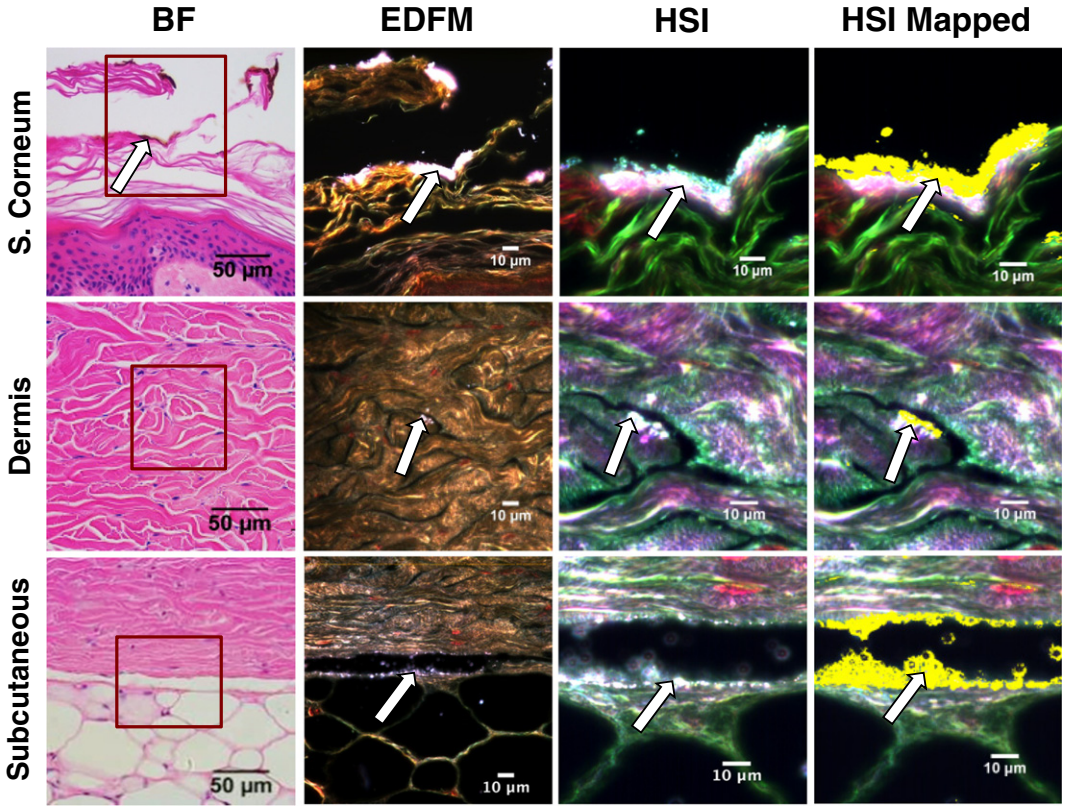


**Fig. 4.** Ceria nanoparticles in porcine skin. Ceria NPs are found in H&E stained skin samples and imaged with different modalities (from left to right: BF, EDFM, HSI, and HSI mapped overlay). From top to bottom, images correspond to *s. corneum*, dermis, and subcutaneous tissue of different samples in the ceria exposure group, respectively. In the BF column (40× magnification), NPs are evident over the *s. corneum*, but they are not evident in the dermis or subcutaneous tissue. The areas enclosed in a red square were imaged with EDFM and HSI (100× magnification). White/pink/purple high contrast areas (arrows) corresponding to the NPs are shown in the EDFM and HSI images, while positive mapping is represented by the yellow overlay in the HSI mapped images.

NP were combined together to create a more robust SL for each type of NP, following the method by Sosa Peña et al., (2016), where the presence of the NP of interest was confirmed by Raman spectroscopy (RS), scanning electron microscopy, and EDX (data reported previously (Sosa Peña et al., 2016)). The "particle filter" tool in the HSI software (ENVI 4.8) was used to create each SL from the regions of interest containing confirmed NPs of interest (Roth et al., 2015c). Each of the combined positive control SLs for each NP type was filtered against several datacubes of the negative controls where no NPs were visualized (NP-free datacubes of epidermis, dermis, and subcutaneous tissue) for the creation of a RSL. This filtering process removes duplicative spectra that are found in both the positive and negative control datacubes; once these duplicative spectra are removed, the RSL contains only the unique spectra found in the positive controls and increases the specificity of the RSL (Roth et al., 2015c). This process was followed for each of the NP types to create a specific RSL for each NP of interest (alumina, ceria, and silica). The RSL for each NP type was used to map against all the datacubes obtained from the experimental samples exposed to the same NP to detect the areas with the same spectral profile as the RSL using the SAM function in the ENVI 4.8 software. The mapped areas were merged together in one classification color and overlaid on the original datacube to observe where the NPs of interest were located within each sample.

### 2.6. Relative quantitation and statistical analysis

For each datacube, the number of pixels with positive mapping to the NP of interest was obtained using the class distribution tool in ENVI 4.8. The number of mapped pixels per total FOV area was obtained for each datacube. In a FOV area of 0.004 $mm^2$ (1 datacube viewed at 100× magnification, with eyepiece lens of 15×), there was a total of 1,000,848 pixels with an area of 4,096 $nm^2$ each (64 nm × 64 nm). The mapping results were obtained in both visual (false coloration overlay on the datacube) and numerical forms (percentage of mapped pixels per datacube).

Statistical analysis was performed using analysis of variance (ANOVA). Calculations were performed with GraphPad Prism version 6.0 statistical software. For each exposure group, 20 samples were analyzed ($n = 20$), and the mean values ± standard error of the mean (SEM) were plotted.

## 3. Results

Use of EDFM-HSI with its SAM feature resulted in identification of NPs in all layers of the skin in all exposed samples. The number of mapped pixels per FOV varied according to the experimental groups. Positive and negative controls were imaged and mapped as shown in Fig. 2. The first column shows the EDFM image of a positive control sample exposed to a NP suspension via injection, where the keratinocytes of the *s. corneum* appear as golden structures (top row). The dermis has a more homogeneous and dense golden coloration and the subcutaneous tissue has a mesh-like light golden appearance. In all cases, NPs are visualized as bright pink/purple specks over the skin tissue (arrows). In some cases, including some EDFM panels in Figs. 2–6, the bright NPs are far more visible in high-resolution images captured at the scope and previewed on the connected computer screen than in smaller, publication-formatted images; larger, higher-resolution images can be found in the Supplementary material (Figs. S2–S6). Even in these cases, the NPs illuminate more clearly in HSI and subsequently appear through mapping, which can be appreciated in these figures. The second column shows same area in the positive control sample viewed under HSI at a higher magnification (100×) and mapped against the RSL for

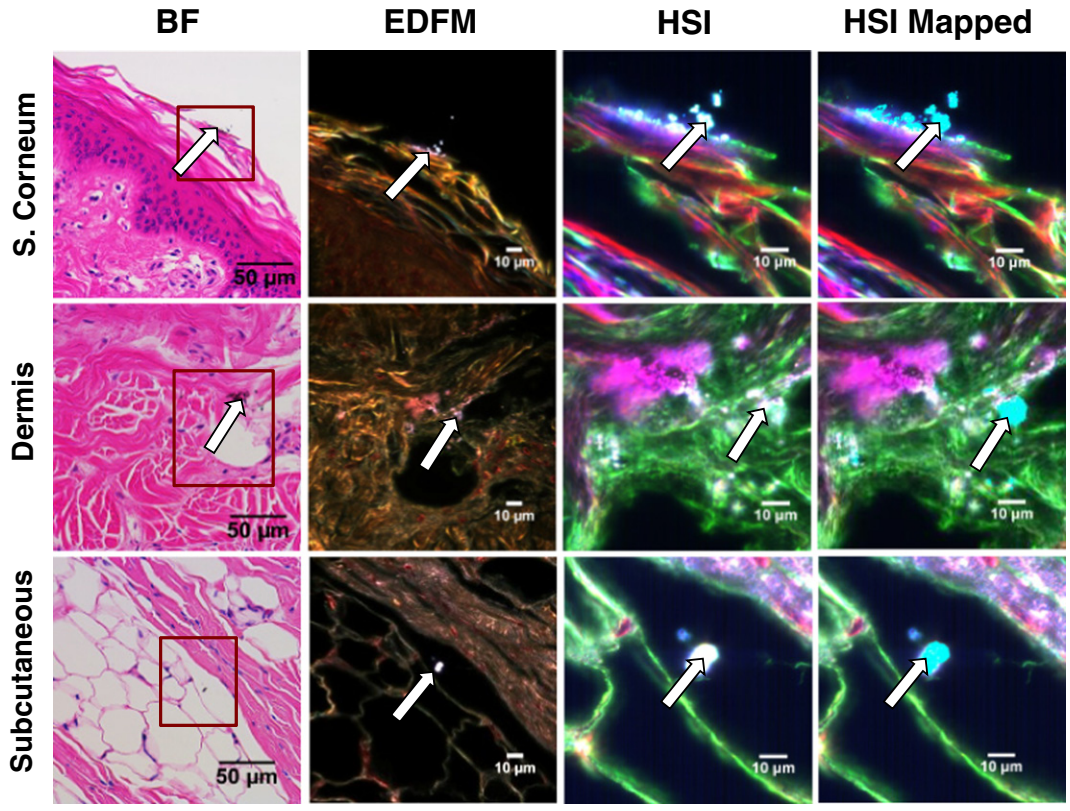


**Fig. 5.** Silica nanoparticles in porcine skin. Silica NPs are found in H&E stained skin samples and imaged with different modalities (from left to right: BF, EDFM, HSI, and HSI mapped overlay). From top to bottom, images correspond to *s. corneum*, dermis, and subcutaneous tissue of different samples in the silica exposure group, respectively. In the BF column (40× magnification), NPs are slightly evident over the *s. corneum* and dermis, but are not evident in the subcutaneous tissue. The areas enclosed in a red square were imaged with EDFM and HSI (100× magnification). Very small white/blue high contrast areas (arrows) corresponding to the NPs are shown in the EDFM and HSI images, while positive mapping is represented by the aqua overlay in the HSI mapped images.

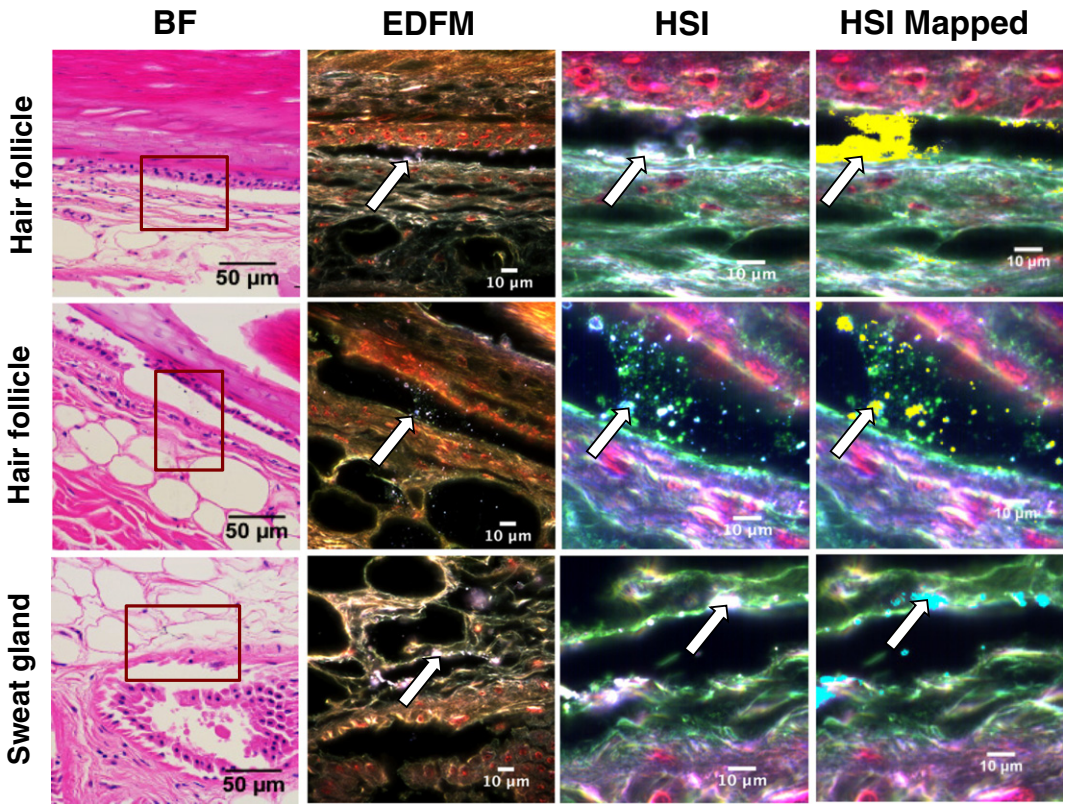


**Fig. 6.** Metal oxide nanoparticles in cutaneous adnexa. Metal oxide NPs are found in H&E stained skin samples and imaged with different modalities (from left to right: BF, EDFM, HSI, and HSI mapped overlay). Top and middle rows correspond to hair follicles found in the dermis of ceria-exposed samples; bottom row corresponds to a sweat gland found in a silica-exposed sample. In the BF images (40× magnification), NPs are either barely evident as dark specks, or not evident at all in the areas enclosed in a red square. Those areas were imaged with EDFM and HSI (100× magnification). In EDFM and HSI very small white/purple/pink high contrast areas (arrows) correspond to the NPs of interest, while positive mapping is represented by the yellow (ceria) and aqua (silica) overlays in the HSI mapped images.

its respective NP group, where the mapped NPs are seen in a distinctive color overlay: ceria is shown in yellow; alumina in blue; and silica in aqua. The third column shows the EDFM image of the negative control for each NP group, where no bright NPs are visualized. The fourth column shows the same negative control sample, imaged with HSI and mapped against the RSL for its respective NP group, where no mapping is present. As expected, positive mapping was observed in the positive control sample and no mapping was observed in the negative control sample.

Positive mapping was observed in all layers of all samples in the experimental groups, as shown in Figs. 3, 4, and 5. Fig. 3 shows images from the alumina exposure group: each row corresponds to a specific layer from different skin samples exposed to the same dose of alumina NPs for the same amount of time. In the *s. corneum*, NPs are seen as white structures over the keratinocytes. In the middle layer, multiple white/pink NPs are agglomerated over the connective tissue in the reticular dermis. In the subcutaneous tissue, the bright pink NPs appear to follow a linear distribution along the dermal/subcutaneous junction. In the third column, the same area was visualized with HSI at 100× magnification, where the NPs are also shown as high contrast areas over the skin tissue (green and red background). The last column shows the HSI image mapped against the alumina RSL, where the mapped areas are shown in a blue overlay. These mapped blue areas represent the alumina NPs found in the tissue that matched the RSL created from the same NPs in the positive control samples.

Tissues from the ceria exposure group are shown in Fig. 4; all the images in this figure correspond to different locations within the same skin sample. In the *s. corneum*, NPs are seen as white structures over the keratinocytes. In the middle layer, a small cluster of white/pink NPs are present over the connective tissue in the reticular dermis. In the bottom subcutaneous tissue, the bright purple NPs follow a linear distribution along the dermal/subcutaneous junction. In the third column, the HSI image also shows the NPs as high contrast areas over the skin tissue (green, red, and purple background). Positive mapping results utilizing the ceria RSL are shown in a yellow overlay in the HSI mapped column. These mapped yellow areas represent the ceria NPs found in the tissue that matched the RSL created from the same NPs in the positive control samples.

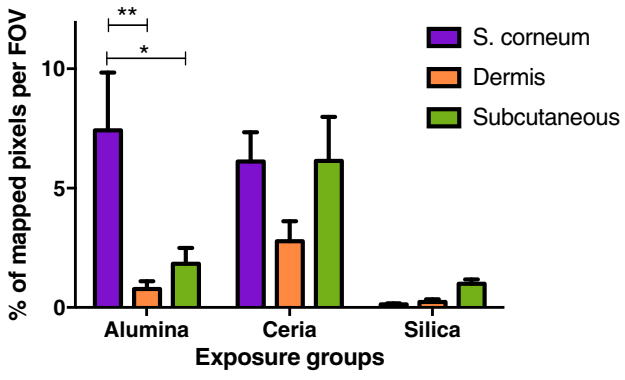


**Fig. 7.** Relative quantitation of nanoparticles per tissue layer expressed as percentage of mapped pixels per FOV. Relative quantitation was obtained by mapping the experimental samples of each group (alumina, ceria, and silica) against their respective RSL. All groups were topically exposed to NPs in aqueous solution for 24 h. An average of mapped pixels per FOV was obtained and separated per layer (*s. corneum*, dermis, or subcutaneous tissue) for each sample. Values are given as mean ± SEM (n = 20). $^{*}p < 0.05$, $^{**}p < 0.01$, $^{***}p < 0.001$, $^{****}p < 0.0001$.

**Table 1**
Relative quantitation of NPs in all exposure groups per tissue layer.

| Exposure group | *S. corneum* (%) | Dermis (%) | Subcutaneous tissue (%) |
|---|---|---|---|
| Alumina | 7.42 | 0.77 | 1.83 |
| Ceria | 6.11 | 2.77 | 6.14 |
| Silica | 0.13 | 0.23 | 0.99 |

A relative quantitation analysis was performed in all the samples of the alumina, ceria, and silica exposure groups. Results are tabulated according to the skin tissue layers, from superficial to deepest layer: *s. corneum*, dermis, and subcutaneous tissue. Results are expressed as percentage of pixels mapped per FOV, using each NP RSL. The data displayed in this table is graphed and statistical significance shown in Fig. 7.

Fig. 5 shows images from the silica exposure group; each row corresponds to different skin samples. With EDFM, in the *s. corneum*, NPs are seen as white granules lying on top of the keratinocytes. In the middle layer, a small agglomeration of white/pink NPs are present over the connective tissue in the reticular dermis. In the subcutaneous tissue, a white cluster of NPs is seen among adipocytes, below the dermal/subcutaneous junction. In the HSI images, NPs are also shown as high contrast areas over the skin tissue. The last column shows the HSI image mapped against the silica RSL, where the mapped areas are shown in an aqua overlay, representing the silica NPs found in the tissue that matched the RSL created from the same NPs in the positive control samples.

Generally, in Figs. 3–5, the NPs found over the *s. corneum* appear to concentrate over the most external layers of the epidermis. The higher concentration of NPs here enables proper standardization of the HSI cataloging of the specific NPs, thereby enabling identification of smaller quantities in other areas of the tissue.

Fig. 6 shows mapped NPs in the dermis adnexa (hair follicles and apocrine sweat glands) of ceria- and silica-exposed samples. To provide visual orientation for these structures, corresponding 4× brightfield images are provided in the Supplementary materials (Figs. S6a, S6c, S6e). In Fig. 6, the first two rows correspond to different hair follicles shown in the same ceria-exposed skin sample, and the bottom row shows the sweat gland of a silica-exposed sample. No NPs were found in the cutaneous adnexa of alumina-exposed samples. In the hair follicles, NPs are seen as white/pink granules lining the junction between the fibro collagenous follicle sheath and the connective tissue in the dermis. In the bottom row, multiple small clusters of white/pink NPs are present lining the connective tissue and adipocytes surrounding an apocrine sweat gland. The last column shows the HSI image mapped against the respective metal oxide RSL, where the mapped areas are shown in a yellow overlay for the ceria and in aqua for silica. These mapped yellow and aqua areas represent the ceria and silica NPs found in the tissue that matched the RSL created from the same NPs in the positive control samples.

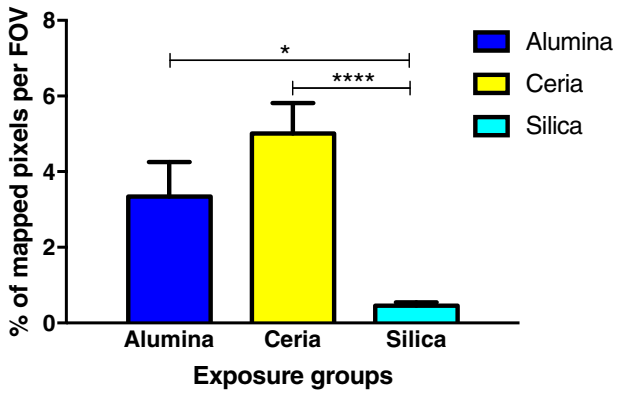


**Fig. 8.** Relative quantitation of nanoparticles per experimental group expressed as percentage of mapped pixels per FOV. Relative quantitation was obtained by mapping the experimental samples of each group (alumina, ceria, and silica) against their respective RSL. All groups were topically exposed to NPs in aqueous solution for 24 h. An average of mapped pixels per FOV was obtained combining all tissue layers for each exposure group. Values are given as mean ± SEM (n = 20). $^{*}p < 0.05$, $^{**}p < 0.01$, $^{***}p < 0.001$, $^{****}p < 0.0001$.

In order to assess NP distribution throughout each sample, a percentage of mapped pixels per FOV was obtained per tissue layer, as shown in Fig. 7. A relative quantitative analysis of the mapped pixels per FOV found in all exposure groups per tissue layer is shown in Table 1 and graphed in Fig. 7. The highest percentage of mapped pixels over the *s. corneum* was found in the alumina-exposed samples, followed by the ceria- then the silica-exposed samples. Lower percentages of mapped pixels were found in the deeper layers in the alumina-exposed group, compared to the superficial layer. In the dermis, ceria had the highest load of NPs, compared to the alumina- and silica-exposed groups. The deepest layer, the subcutaneous fat, had the highest concentration in the ceria-exposed group, compared to the other two groups. From these data, statistically significant differences were found when comparing the percentage of mapped pixels over the *s. corneum* and the dermis ($p < 0.01$), and when comparing the *s. corneum* and the subcutaneous tissue ($p < 0.05$) in the alumina group. No statistically significant difference was found when comparing the different layers within the ceria- and silica-exposed groups (Fig. 7).

Combining all tissue layers, the total percentage of mapped pixels per FOV was obtained for all experimental groups (Fig. 8). The highest percentage of mapped pixels (representing NPs) was seen in the ceria-exposed samples, compared to the alumina- and silica-exposed samples. Statistically significant difference was found when comparing the alumina- and silica-exposed groups ($p < 0.05$), and when comparing the ceria- and silica-exposed groups ($p < 0.0001$). On average, the percentage of mapped pixels per FOV for each NP, independent from tissue layers, was as follows: 5.01% (SEM ± 0.80) for ceria, 3.34% (SEM ± 0.91) for alumina and 0.45% (SEM ± 0.08) for silica.

## 4. Discussion

It should be emphasized that this study successfully demonstrates a non-destructive method for direct visualization and relative quantitative analysis of NPs in biological samples by combining EDFM and hyperspectral mapping; it does not lead to conclusions regarding the toxicity of the specific NPs utilized for the purpose of demonstrating the method. Traditional methods for NP quantitation in biological samples have been reviewed (Vanhecke et al., 2014; Sosa Peña et al., 2016; Lopez-Serrano et al., 2014) These methods include inductively coupled plasma mass spectrometry (ICP-MS), which has low detection limits (below one part per trillion) and can analyze metal and non-metal elements and isotopes; however, it requires destructive sample preparation and does not allow for a visual assessment of NP distribution within a given sample (Berezin, 2014). ICP-OES is similar and complementary to ICP-MS, with even lower detection limits, but cannot distinguish between particles that are bound or in free form due to the digestion process for biological samples (Berezin, 2014). Laser-induced breakdown spectroscopy (LIBS) determines elemental composition and allows for a non-destructive and label-free compositional and quantitative NP analysis using a pulsed laser, but it does not differentiate between different NP sizes or compositions, and its quantitative analysis is affected by the changes in intensity emission caused by different matrices (Anabitarte et al., 2012). Other quantitation methods utilizing imaging tools have also been attempted at a single cell level by utilizing confocal fluorescence with image analysis software (Torrano et al., 2013), by combining stereological sampling techniques with transmission EM (Elsaesser et al., 2011) and by using different standard spectrophotometers (Unciti-Broceta et al., 2015). These methods require more intensive sample preparation than EDFM-HSI and do not provide better quantitative data than the spectrometry methods.

Additionally, there are other methods for NP quantitation for environmental sampling that take into account the specific properties of certain NPs. For example, near infrared fluorescence (NIRF) spectroscopy has been used for single-walled carbon nanotubes (SWCNT) in

sediment, biota, and aqueous solutions based on its fluorescence and absorbance properties (Schierz et al., 2012), programmed thermal analysis for SWCNTs and MWCNTs in cyanobacteria and urban air based on their thermal properties (Doudrick et al., 2012), and $^{14}$-C isotropic quantitation for few layer graphene (FLG) in aquatic organisms based on its oxidation and reaction byproducts (Feng et al., 2015); however, none of these methods are without their own limitations. For nanomaterials with high reflectance properties, such as the metal oxides used in this study, EDFM-HSI is a very valuable tool that enhances the natural properties of those NPs for facilitating detection while allowing for characterization and relative quantitation.

While spectrometry methods provide reliable quantitation for NPs in biological samples (e.g., total organ burden), it is also valuable, from a toxicological standpoint, to know where in the sample these NPs concentrate, what shape or form they acquire when in contact with the tissue, and if there is a tendency for those NPs to concentrate around systemic distribution routes, as opposed to a random distribution. This information can be provided by direct visualization methods like EDFM-HSI. While inferior to spectrometry for absolute quantitation, EDFM-HSI offers added value by providing relative quantitative analysis in combination with visual and anatomical information, including localization of NPs within a sample. This method also allows for comparison between different tissue layers within the same and different exposure groups, thus enabling relative quantitation of NP abundance. It is important to note that while the methods demonstrated in this study may be applied and adapted to facilitate the investigation of toxicological endpoints as well as NP biodistribution, it was not designed to yield conclusions regarding the toxicity of the specific NPs utilized to demonstrate these methods.

Since the samples utilized for this study were prepared for conventional light microscopy and thus can be further examined by a pathologist to assess structural and other changes, the utility of this tool in the diagnostic world may surpass other similar modalities. We used the standard approach used by pathologists of adding multiple image frames to obtain a relative quantitation of NPs as a percentage of mapped pixels per FOV in immunohistochemistry (IHC) samples (Rizzardi et al., 2012). One difference was that EDFM visualization does not require IHC or any special staining, as the high contrast produced by the NPs of interest is clearly identified with EDFM; however, staining may be necessary for additional analytical techniques, such as the comparison to BF microscopy shown here. Also of note, EDFM revealed NPs by direct visualization, which were not readily seen using BF microscopy for the same sample. The potential for using the same histological sample to easily identify NPs, assess NP biodistribution, and provide a relative quantitation of NP abundance, while retaining the option for further study by a trained pathologist, holds great promise for both toxicology and medicine.

While the primary goal of this paper was to provide a method for relative quantitation of NPs in histological samples in a non-destructive manner, the methods presented here could be applied and adapted to help answer questions in future toxicological skin penetration studies, such as whether the *s. corneum* is an effective barrier for the translocation of NPs from the superficial to the deeper layers. Moreover, these methods can be utilized to obtain relative quantitation for other exposure models, allowing for non-damaging and dye-free tissue preparation techniques.

### 4.1. Limitations

While EDFM-HSI can rapidly detect NPs, a limitation is its inability to obtain the absolute NP count, as its low spatial resolution cannot differentiate between single NPs and agglomerates (Roth et al., 2015b, 2015c). Although there are various benefits from using EDFM-HSI over EM, particularly in time- and cost-reduction, some challenges still exist for these tools in terms of achieving a relative quantitative assessment of the studied samples. While EM can detect, quantify and characterize single NPs, the low spatial resolution of EDFM-HSI cannot identify single particles and cannot determine the number of individual NPs in an agglomerate. It may, however, allow for relative quantitation of NP clusters or agglomerations in biological samples, including histological tissues, where agglomerations have been extensively and consistently reported (Mercer et al., 2013; Anderson et al., 2015), or when a relative quantitation based on the percentage of pixels mapped is sufficient.

## 5. Conclusions

The methods presented here, utilizing EDFM-HSI, provided a relative quantitative analysis and valuable information about biodistribution of NPs in histological samples with no destruction of the tissue and no labels required. In a skin penetration model specifically engineered for very small volume exposures, relative quantitation of NPs with EDFM-HSI has proven to be useful to compare NP abundance between different exposure groups and between different tissue layers. This method therefore holds value for applications in toxicological, exposure, medical, and other biological studies utilizing nanoscale materials. However, in order to apply the method presented here to other NPs and/or to investigate toxicological or other biological endpoints, this relative quantitative analysis may require adaptation and should be replicated with a greater number of samples to generate significant statistical analysis. These methods could be used for other classes and categories of NPs in a wide range of biological and environmental matrices, thus broadening the impact and utility of these methods across disciplines such as toxicology, pharmacology, medicine, occupational health, and environmental science.

## Funding

This work was supported by CDC-NIOSH [grant OH-009990-01A1] awarded to S.B. and the NanoHealth and Safety Center, New York State, awarded to S.B., A.F., and M.F. The contents of this publication are solely the responsibility of the authors and do not necessarily represent the official views of the CDC-NIOSH or New York State.

## Acknowledgments

The authors thank Rani Sellers, DVM, PhD and Barbara Cannella, PhD (Albert Einstein College of Medicine Histology and Comparative Pathology Facility) for sample preparation. The authors also thank the Biomedical Engineering Senior Design Team at Stony Brook University – Matthew Chase, Jeonghun Choi, Kushagra Singhal, and Jeffrey Zinke – for the final design and construction of the modified Franz diffusion chamber used in this study.

## Appendix A. Supplementary data

Supplementary data to this article containing nanoparticle characterization data and high resolution images, can be found online at http://dx.doi.org/10.1016/j.impact.2016.09.006.

## References

Aalderink, B.J., Klein, M.E., Padoan, R., et al., 2009. Clearing the image: a quantitative analysis of historical documents using hyperspectral measurements. B Pap. Gr. Annu. 28, 115–120.
Adachi, K., Yamada, N., Yoshida, Y., et al., 2013. Subchronic exposure of titanium dioxide nanoparticles to hairless rat skin. Exp. Dermatol. 22, 278–283.
Adamcakova-Dodd, A., Stebounova, L.V., Kim, J.S., et al., 2014. Toxicity assessment of zinc oxide nanoparticles using sub-acute and sub-chronic murine inhalation models. Part. Fibre Toxicol. 11, 15.
Anabitarte, F., Cobo, A., Lopez-Higuera, J.M., 2012. Laser-induced breakdown spectrosocpy: fundamentals, applications, and challenges. ISRN Spectrosc. 1–12.
Anderson, D.S., Patchin, E.S., Silva, R.M., et al., 2015. Influence of particle size on persistence and clearance of aerosolized silver nanoparticles in the rat lung. Toxicol. Sci. 144, 366–381.

Badireddy, A.R., Wiesner, M.R., Liu, J., 2012. Detection, characterization, and abundance of engineered nanoparticles in complex waters by hyperspectral imagery with enhanced darkfield microscopy. Environ. Sci. Technol. 46, 10081–10088.
Baroli, B., Ennas, M.G., Loffredo, F., et al., 2007. Penetration of metallic nanoparticles in human full-thickness skin. J. Invest. Dermatol. 127, 1701–1712.
Berezin, M. (Ed.), 2014. Nanotechnology for Biomedical Imaging and Diagnostics: From Nanoparticle Design to Clinical Applications. Wiley.
Brenner, S.A., Neu-Baker, N.M., 2014. Occupational exposure to nanomaterials: assessing the potential for cutaneous exposure to metal oxide nanoparticles in a semiconductor facility. J. Chem. Health Saf. 22, 10–19.
Brenner, S.A., Neu-Baker, N.M., Caglayan, C., et al., 2016. Occupational exposure to airborne nanomaterials: an assessment of worker exposure to aerosolized metal oxide nanoparticles in a semiconductor fab and subfab. J. Occup. Environ. Hyg. 13 (9), D138–D147.
Contado, C., 2015. Nanomaterials in consumer products: a challenging analytical problem. Front. Chem. 3, 48.
da Silva, A.R., Aucelio, R.Q., Rodriguez-Cotto, R.I., et al., 2014. Physicochemical properties and toxicological assessment of modified CdS nanoparticles. J. Nanopart. Res. 16, 2655.
Darwiche, K., Zarogoulidis, P., Krauss, L., et al., 2013. "One-stop shop" spectral imaging for rapid on-site diagnosis of lung cancer: a future concept in nano-oncology. Int. J. Nanomedicine 8, 4533–4542.
Doudrick, K., Herckes, P., Westerhoff, P., 2012. Detection of carbon nanotubes in environmental matrices using programmed thermal analysis. Environ. Sci. Technol. 46, 12246–12253.
Elsaesser, A., Barnes, C.A., McKerr, G., et al., 2011. Quantificaiton of nanoparticle uptake by cells using an unbiased sampling method and electron microscopy. Nanomedicine 6, 1189–1198.
England, C.G., Huang, J.S., James, K.T., et al., 2015. Detection of phosphatidylcholine-coated gold nanoparticles in orthotopic pancreatic adenocarcinoma using hyperspectral imaging. PLoS One 10, e0129172.
European Academies Science Advisory Council (EASAC), 2011. Impact of Engineered Nanomaterials on Health: Considerations for Benefit-Risk Assessment. Publications Office of the European Union, Luxembourg.
Feng, Y., Lu, K., Mao, L., et al., 2015. Degradation of $^{14}$C-labeled few layer graphene via Fenton reaction: reaction rates, characterization of reaction products, and potential ecological effects. Water Res. 84, 49–57.
Fröhlich, E., Salar-Behzadi, S., 2014. Toxicological assessment of inhaled nanoparticles: role of in vivo, ex vivo, in vitro, and in silico studies. Int. J. Mol. Sci. 15, 4795–4822.
Global Industry Analysts, 2010. Global market for nanotechnology-enabled products to reach US $2.41 trillion by 2015. According to a New Report by Global Industry Analysts, Inc., pp. 2–5
Grabinski, C., Schlager, J., Hussain, S., 2013. Hyperspectral microscopy for characterization of gold nanoparticles in biological media and cells for toxicity assessment. Nanomater. Interfaces Biol. 1025, 167–178.
Husain, M., Wu, D., Saber, A.T., et al., 2015. Intratracheally instilled titanium dioxide nanoparticles translocate to heart and liver and activate complement cascade in the heart of C57BL/6 mice. Nanotoxicology 9, 1013–1022.
Kessler, R., 2011. Engineered nanoparticles in consumer products: understanding a new ingredient. Environ. Health Perspect. 119, A120–A125.
Klein, M.E., Aalderink, B.J., Padoan, R., et al., 2008. Quantitative hyperspectral reflectance imaging. Sensors 8, 5576–5618.
Krishnaraj, C., Harper, S.L., Yun, S.I., 2016. In vivo toxicological assessment of biologically synthesized silver nanoparticles in adult Zebrafish (*Danio rerio*). J. Hazard. Mater. 301, 480–491.
Kumar, G., Kiernan, J. (Eds.), 2010. Special Stains and H&E. Dako North America, California.
Lopez-Serrano, A., Olivas, R.M., Landaluze, J.S., et al., 2014. Nanoparticles: a global vision. Characterization, separation, and quantification methods. Potential environmental and health impact. Anal. Methods 6, 38–56.
Mercer, R.R., Scabilloni, J.F., Hubbs, A.F., et al., 2013. Extrapulmonary transport of MWCNT following inhalation exposure. Part. Fibre Toxicol. 10, 13.
Mortimer, M., Gogos, A., Bartolomé, N., et al., 2014. Potential of hyperspectral imaging microscopy for semi-quantitative analysis of nanoparticle uptake by protozoa. Environ. Sci. Technol. 48, 8760–8767.
Nel, A.E., Parak, W.J., Chan, W.C.W., et al., 2015. Where are we heading in nanotechnology environmental health and safety and materials characterization? ACS Nano 9, 5627–5630.
Oberdörster, G., Oberdörster, E., Oberdörster, J., 2005. Nanotoxicology: an emerging discipline evolving from studies of ultrafine particles. Environ. Health Perspect. 113, 823–839.
Rizzardi, A.E., Johnson, A.T., Vogel, R.I., et al., 2012. Quantitative comparion of immunohistochemical staining measured by digital image analysis versus pathologist visual scoring. Diagn. Pathol. 7, 42.
Roco, M.C., Mirkin, C.A., Hersam, M.C., 2010. Nanotechnology research directions for societal needs in 2020 - retrospective and outlook. WTEC-World Technol. Eval. Cent. 476–477.
Roth, G.A., Neu-Baker, N.M., Brenner, S.A., 2015a. SEM analysis of particle size during conventional treatment of CMP process wastewater. Sci. Total Environ. 508, 1–6.
Roth, G.A., Tahiliani, S., Neu-Baker, N.M., et al., 2015c. Hyperspectral microscopy as an analytical tool for nanomaterials. Wiley Interdiscip. Rev. Nanomed. Nanobiotechnol. 7, 565–579.
Roth, G.A., Sosa Peña, M.P., Neu-Baker, N.M., et al., 2015d. Identification of metal oxide nanoparticles in histological samples by enhanced darkfield microscopy and hyperspectral mapping. J. Vis. Exp. 106, e53317.
Roth, G.A., Neu-Baker, N.M., Brenner, S.A., 2015b. Comparative charaterization methods for metal oxide nanoparticles in aqueous suspensions. J. Chem. Health Saf. 22, 26–32.
Schierz, A., Parks, A.N., Washburn, K.M., et al., 2012. Characterization and quantitative analysis of single-walled carbon nanotubes in the aquatic environment using near-infrared fluorescence spectroscopy. Environ. Sci. Technol. 46, 12262–12271.
Schneider, M., Stracke, F., Hansen, S., et al., 2009. Nanoparticles and their interactions with the dermal barrier. Dermatoendocrinol. 1, 197–206.
Shepard, M., Brenner, S., 2014a. Cutaneous exposure scenarios for engineered nanoparticles used in semiconductor fabrication: a preliminary investigation of workplace surface contamination. Int. J. Occup. Environ. Health 20, 247–257.
Shepard, M.N., Brenner, S., 2014b. An occupational exposure assessment for engineered nanoparticles used in semiconductor fabrication. Ann. Occup. Hyg. 58, 251–265.
Singh, P., Nanda, A., 2014. Enhanced sun protection of nano-sized metal oxide particles over conventional metal oxide particles: an in vitro comparative study. Int. J. Cosmet. Sci. 36, 273–283.
Sonavane, G., Tomoda, K., Sano, A., et al., 2008. In vitro permation of gold nanoparticles through rat skin and rat intestine: effect of particle size. Colloids Surf. B: Biointerfaces 65, 1–10.
Sosa Peña, M.P., Gottipati, A., Tahiliani, S., et al., 2016. Hyperspectral imaging of nanoparticles in biological samples: simultaneous visualization and elemental identification. Microsc. Res. Tech. 79 (5), 349–358.
Sykes, E.A., Dai, Q., Tsoi, K.M., et al., 2014. Nanoparticle exposure in animals can be visualized in the skin and analysed via skin biopsy. Nat. Commun. 5, 3796.
Titford, M., 2009. Progress in the development of microscopical techniques for diagnostic pathology. J. Histotechnol. 32, 9–19.
Torrano, A.A., Blechinger, J., Osseforth, C., et al., 2013. A fast analysis method to quantify nanoparticle uptake on a single cell level. Nanomedicine 8, 1815–1828.
U.S. CDC-NIOSH, 2009. Approaches to Safe Nanotechnology: Managing the Health and Safety Concerns Associated with Engineered Nanomaterials DHHS (NIOSH) Publication No. 2009–125 .
Unciti-Broceta, J.D., Cano-Cortés, V., Altea-Manzano, P., et al., 2015. Number of nanoparticles per cell through a spectrophotometric method - a key parameter to assess nanoparticle-based cellular assays. Sci. Rep. 5, 10091.
Vanhecke, D., Rodriguez-Lorenzo, L., Clift, M.J.D., et al., 2014. Quantification of nanoparticles at the single-cell level: an overview about state-of-the-art techniques and their limitations. Nanomedicine 9, 1885–1900.
Zvyagin, A.V., Zhao, Z., Gierden, A., et al., 2008. Imaging of zinc oxide nanoparticle penetration in human skin in vitro and in vivo. J. Biomed. Opt. 13, 1–9.